

See discussions, stats, and author profiles for this publication at: <https://www.researchgate.net/publication/282978353>

Bifunctional $\text{Ce}_{1-x}\text{Eu}_x\text{O}_2$ ($0 \leq x \leq 0.3$) nanoparticles for photoluminescence and photocatalyst applications: An X-ray absorption spectroscopy study

ARTICLE in PHYSICAL CHEMISTRY CHEMICAL PHYSICS · OCTOBER 2015

Impact Factor: 4.49 · DOI: 10.1039/c5cp05251c

READS

24

4 AUTHORS, INCLUDING:



Aditya Sharma

Pohang University of Science and Technology

33 PUBLICATIONS 98 CITATIONS

SEE PROFILE



Mayora Varshney

Pohang Accelerator Laboratory

26 PUBLICATIONS 62 CITATIONS

SEE PROFILE



Hyun-Joon Shin

Pohang University of Science and Technology

170 PUBLICATIONS 2,645 CITATIONS

SEE PROFILE

PCCP

Accepted Manuscript



This article can be cited before page numbers have been issued, to do this please use: A. Sharma, M. Varshney, J. Park, T. K. Ha, H. Shin and K. H. Chae, *Phys. Chem. Chem. Phys.*, 2015, DOI: 10.1039/C5CP05251C.



This is an *Accepted Manuscript*, which has been through the Royal Society of Chemistry peer review process and has been accepted for publication.

Accepted Manuscripts are published online shortly after acceptance, before technical editing, formatting and proof reading. Using this free service, authors can make their results available to the community, in citable form, before we publish the edited article. We will replace this *Accepted Manuscript* with the edited and formatted *Advance Article* as soon as it is available.

You can find more information about *Accepted Manuscripts* in the [Information for Authors](#).

Please note that technical editing may introduce minor changes to the text and/or graphics, which may alter content. The journal's standard [Terms & Conditions](#) and the [Ethical guidelines](#) still apply. In no event shall the Royal Society of Chemistry be held responsible for any errors or omissions in this *Accepted Manuscript* or any consequences arising from the use of any information it contains.

Bifunctional $\text{Ce}_{1-x}\text{Eu}_x\text{O}_2$ ($0 \leq x \leq 0.3$) nanoparticles for photoluminescence and photocatalyst applications: An X-ray absorption spectroscopy study

Aditya Sharma,^{a*} Mayora Varshney^a, Jaehun Park^a, Tae Kyun Ha^a, Keun Hwa Chae^b, and Hyun Joon Shin^{a*}

Received 00th January 20xx,
Accepted 00th January 20xx

DOI: 10.1039/x0xx00000x

www.rsc.org/

$\text{Ce}_{1-x}\text{Eu}_x\text{O}_2$ ($0 \leq x \leq 0.3$) nanoparticles (NPs) were synthesized by chemical precipitation method. The microstructures and morphology were characterized by the synchrotron X-ray diffraction and high resolution transmission electron microscopy. X-ray absorption near edge structure (XANES) spectra at the Eu $\text{M}_{5,4}$ -edge and atomic-multiplet calculations revealed that the Eu^{+3} was predominantly present in CeO_2 lattice and Eu^{+2} was negligibly present within the entire doping range. The detailed analysis of the Ce $\text{M}_{5,4}$ -edge and the O K-edge has shown strong dependence of $\text{Ce}^{+3}/\text{Ce}^{+4}$ ratio and oxygen vacancy with Eu content. Extended X-ray absorption fine structure (EXAFS) spectra at the Ce K-edge, along with theoretical fitting, have shown systematic variation in the coordination number, bond length and Debye-Waller factor with Eu doping. A blue shift in the absorption edge was observed which implies a net increase in the charge transfer gap between the O $2p$ and Ce $4f$ bands due to the increased number of Ce^{+3} ions in the Eu doped samples. The excitation and emission spectra of pure CeO_2 NPs did not show any photoluminescence (PL) characteristic; however, $\text{Ce}_{1-x}\text{Eu}_x\text{O}_2$ ($x = 0.1-0.3$) NPs showed significant improvement in the $4f-4f$, $^5\text{D}_0 - ^7\text{F}_2$ and $^5\text{D}_0 - ^7\text{F}_1$ transitions induced luminescence properties. Eu doping has two major effects on the electronic structure and optical properties of CeO_2 NPs: The first, at an Eu content of 10 mol%, is the formation of $\text{Ce}^{+4} - \text{O} - \text{Eu}^{+3}$ networks, i.e., Eu^{+3} ions substitute the Ce^{+4} ions and introduce oxygen vacancies and Ce^{+3} ions in the host lattice which favors the $^5\text{D}_0 - ^7\text{F}_2$ induced PL properties. The other, at an Eu doping over 10 mol%, is the formation of both $\text{Ce}^{+4} - \text{O} - \text{Eu}^{+3}$ and $\text{Ce}^{+3} - \text{O} - \text{Eu}^{+3}$, i.e., Eu^{+3} ions not only take substitutional sites of Ce^{+4} ions but also replace a fraction of Ce^{+3} ions in the CeO_2 lattice which favors $^5\text{D}_0 - ^7\text{F}_1$ induced PL properties. As an application of CeO_2 NPs towards the degradation of water pollutants, we demonstrated that the $\text{Ce}_{1-x}\text{Eu}_x\text{O}_2$ ($0 \leq x \leq 0.3$) NPs can serve as effective photocatalyst materials towards the degradation of methyl-orange aqueous pollutant dye under UV light irradiation.

Introduction

In responding to the needs of modern science/technology and emerging environmental concerns, it is important to investigate those materials which are inexpensive, environment friendly and multifunctional. In this context, metal-oxide nanoparticles (NPs) are promising for their multifunctional behaviour because they often exhibit superior chemical/physical properties and potentially functional in a broad range of applications. However, the performance of such materials is highly sensitive to their size, shape, electronic structure and structural properties¹⁻⁴. Among the known metal oxide semiconductors, the CeO_2 , as a rare earth metal oxide, has gained a great attention in a wide range of applications, such as solar-cells¹, gas-sensing⁵, oxide fuel cells⁶, automotive catalyst⁷, ultraviolet shielding⁸, etc. Efforts also have been made to explore the biomedical applications of CeO_2 as a radical scavenging antioxidant⁹. CeO_2 can protect the healthy cells from the radiation-induced

damage during the radiation therapy and provides neuroprotection to the spinal cord neurons¹⁰⁻¹¹. Thus, the excellent biocompatibility and nontoxic nature of CeO_2 can make it a potential candidate in many of the biomedical applications; however, it exhibits weak emission characteristics that limit its applications in the cellular and biological studies. In this regard, various rare earth elements, like Er^{+3} , Eu^{+3} , Sm^{+3} and Tb^{+3} , have been incorporated in the host lattice to improve the photoluminescence (PL) property of weakly emitting CeO_2 NPs¹²⁻¹⁶. However, emission mechanism in these systems is still controversial and is greatly dependent on the synthesis techniques and concentration of lattice defects.

Azo dyes (e.g., Methyl orange (MO)) are widely used in the pharmaceutical, printing, textile and research laboratories. Such dyes can enter into a human body through skin/mouth and can cause vomiting, fast heart rate and death of lung tissues. Therefore, such azo dyes must be degraded into their subdomains, which are less/non-toxic, before they are released into river/sea water. CeO_2 exhibits strong light absorption in the UV region, presents high redox potential of $\text{Ce}^{+4} - \text{Ce}^{+3}$ couples and possesses high resistance to chemical or photo corrosion. Thus, the CeO_2 NPs can be utilized in the photocatalytic degradation of various azo dyes¹⁷. Therefore, in order to explore the pure and doped CeO_2 NPs for their improved

^a Pohang Accelerator Laboratory (POSTECH) Pohang-790784, South Korea. *Email: shj001@postech.ac.kr, adityaiuac@gmail.com Fax: +82-54279-1599; Tel: +82-54279-1767

^b Advanced Analysis centre, Korea Institute of Science and Technology, Seoul-136-791, South Korea

ARTICLE

PCCP

functionality in the technological fields and environmental safety, systematic research efforts are desired with deep understanding of their structural, optical, electronic structure, and catalyst properties.

In most of the previous reports, X-ray photoelectron spectroscopy (XPS) has been employed on the pure and doped CeO_2 NPs to determine the concentration and oxidation state of metal ions^{13–16}. Although this technique provides information regarding the oxidation state of the probed ion in certain thin samples, (i) it is mainly surface probing technique (ii) and may undergo severe charging effects during the collection of XPS data. Therefore, other element specific techniques which are rather straightforward and modest, like X-ray absorption spectroscopy (XAS), within the low and high energy range may be advantageous to investigate the local atomic structure, coordination number, valence state and hybridization of the probed elements. Here, we take advantage of the synchrotron light source based X-ray absorption near edge structure (XANES) and extended X-ray absorption fine structure (EXAFS) spectroscopy techniques, which can probe the density of states, to reveal the effect of Eu doping on the defect/electronic structure modulated PL and photocatalytic performance of the $\text{Ce}_{1-x}\text{Eu}_x\text{O}_2$ ($0 \leq x \leq 0.3$) NPs. We demonstrate that the Eu^{+3} takes substitutional sites in the host CeO_2 lattice, without formation of trivial oxide phases, and facilitates oxygen ion vacancies and $\text{Ce}^{+4}-\text{O}-\text{Eu}^{+3}$ and $\text{Ce}^{+3}-\text{O}-\text{Eu}^{+3}$ networks which favour the photoluminescence properties of the compound. It is also observed that the Eu doping induced modified electron density can improve photocatalytic performance of NPs, leading to degradation of MO aqueous dye under the light irradiation, manifesting the synthesis of bifunctional $\text{Ce}_{1-x}\text{Eu}_x\text{O}_2$ NPs in the present study.

Experimental details

$\text{Ce}_{1-x}\text{Eu}_x\text{O}_2$ ($x = 0.0$ to 0.3) nanoparticles were synthesized by using previously stabilized chemical precipitation method^{18–19}. All the reagents used were of analytical grade without further purification. 0.01M solutions of $\text{Ce}(\text{CH}_3\text{COO})_3 \cdot 5\text{H}_2\text{O}$ and $\text{Eu}(\text{CH}_3\text{COO})_3 \cdot \text{H}_2\text{O}$ were prepared with a molar ratio of $x = \text{Eu}/(\text{Ce}+\text{Eu})$ by dissolving them into de-ionized (DI) water. Ammonium hydroxide (NH_4OH) was added into the solution (drop by drop) under the magnetic stirring to form the white precipitates of $\text{Ce}_{1-x}\text{Eu}_x\text{O}_2$. The pH value during the reaction was kept constant, $\text{pH} = 9$, for all the compositions. The resultant precipitates were washed several times with DI water to remove organic impurities. The precipitates were heated in air at 80°C for 30 h followed by natural cooling up to room temperature and, finally, the light yellow coloured powders were collected. For identifying the crystal structure of as-synthesized nanoparticles, the synchrotron X-ray diffraction ($\lambda = 1.240 \text{ \AA}$) measurements were performed at X-ray scattering beam line [3D beam line of Pohang Accelerator laboratory (PAL), South Korea]. The morphology and size of NPs were studied with JOEL-JEM-2200FS high resolution transmission electron microscope (HR-TEM) accompanied with selected area electron diffraction (SAED). To prepare the samples for the HR-TEM measurements, the powder samples were fairly dispersed in the ethanol solution using sonication for 20 min and then the suspended NPs were drop-wise loaded on carbon film coated Cu grids. XANES spectra at the Eu $\text{M}_{5,4}$ -edge, O K-edge, and Ce $\text{M}_{5,4}$ -edge were collected in total electron yield (TEY) mode at the 10D (PAL-KIST) beam line of PAL. The photon

energy resolution of this beam line was better than 0.6 eV (at the O K-edge). The XANES measurements at the Ce K-edge and Eu L-edge were collected at the 10 C beam line of PAL. This beam line has high flux and wide energy range with a Si (311) double crystal monochromator. Three ionization chambers, filled with Ar gas, were used to record the intensity of the incident (I_0) and the transmitted (I_t) X-rays (the sample was placed between the first and the second ionization chamber). The PL excitation and emission spectra were recorded by using the Varian-Cary eclipse fluorescence spectrophotometer equipped with a 150 W xenon lamp as excitation source. For the evaluation of photocatalytic activity of the samples, towards the degradation of MO solution, systematic UV-visible absorption spectra were collected from the samples at different time of light irradiation. To establish the adsorption-desorption reactions of pollutant dye molecules on the catalyst samples surface, 0.2 g of the as-synthesized $\text{Ce}_{1-x}\text{Eu}_x\text{O}_2$ NPs were fairly dispersed in the 100 ml of previously prepared MO aqueous solution (0.1g/L) in the dark for 45 minutes under the magnetic stirring. A commercial 100 W mercury lamp was used as the light source to irradiate the samples. After regular irradiation intervals (30 min), 20 ml of the suspensions were sampled and then the NPs were separated by centrifugation. The degradation of MO dye was determined by collecting the UV-visible absorption spectra using a Varian Cary-100 UV-visible spectrophotometer.

Results and discussion

XRD and TEM study

Figure 1 shows the XRD patterns of $\text{Ce}_{1-x}\text{Eu}_x\text{O}_2$ ($x = 0.0$ to 0.3) samples. All of the XRD spectra were analysed by *Powder X* software. The diffraction patterns of all the samples were fairly resembled to the cubic fluorite structure of CeO_2 with space group $\text{-Fm}\bar{3}\text{m}$ (JCPDS# 34-0394). No diffraction peaks from the impurity phases, such as Ce_2O_3 , Eu_2O_3 , EuO etc., could be detected within the detection limit of used X-ray diffractometer.

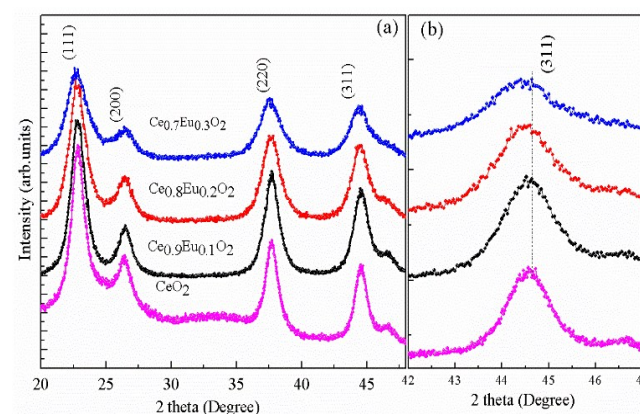


Fig.1 (Colour online) XRD patterns of $\text{Ce}_{1-x}\text{Eu}_x\text{O}_2$ ($x=0.0-0.3$) NPs. Fig. 1(b) shows the closer view of the (311) peak. The spectra are vertically shifted for a clearer view.

This indicates that the Eu dopant does not segregate, in the entire doping range, but occupy the Ce sites in the CeO₂ lattice. In the other oxides (e.g., Y₂O₃ and Gd₂O₃), the solubility limit of Eu was only up to 3.5 to 5 mol.% leading to the segregation of Eu oxide phases and resulting in the quenching of PL properties^{20, 21}. In the present case, both the Ce and Eu belong to the lanthanide series and exhibit higher solubility¹⁴, and, therefore, Eu is expected to be dispersed throughout the CeO₂ lattice even at relatively higher Eu (30 mol.%) concentration. Formation of Eu oxide phase was observed in the 40 mol% Eu doped CeO₂ NPs (not shown here) owing to the solubility limit of Eu in CeO₂ matrix using the present synthesis method and given experimental conditions. The average particle size of CeO₂:Eu NPs was calculated using the Scherrer relation; $D = 0.9\lambda / \beta \cos\theta$, where λ is the wavelength of used X-rays and β is the full width at half maximum of the XRD peaks. Thus estimated particle size is ~ 6.2 nm, ~ 5.4 nm, ~ 4.8 nm and ~ 4.1 nm for CeO₂, Ce_{0.9}Eu_{0.1}O₂, Ce_{0.8}Eu_{0.2}O₂ and Ce_{0.7}Eu_{0.3}O₂ samples, respectively. Similar decrease in the particle size has also been reported in the Hf and Zr doped CeO₂¹⁹ NPs and Eu doped TiO₂²² NPs, because the doping of foreign elements induces local distortion in the crystalline lattice and restricts the long range ordering. Fig. 1 (b) shows that there is peak (e.g., (311) peak) broadening and marginal peak shift towards the lower diffraction angle. Several possibilities can explain the XRD peak shift and peak broadening; like, decrease in the particle size and distortion in the crystal structure, etc. Here, the ionic radii of Ce⁴⁺ ions is quite smaller (Ce⁴⁺ = 0.097 nm) than that of Eu⁺³ or Eu⁺² ions (i.e., Eu⁺³ = 0.106 nm and Eu⁺² = 0.129 nm). Therefore, any substitution of Ce⁴⁺ by Eu⁺³ or Eu⁺² may enlarge the interatomic spacing of the cubic cell of CeO₂ which is reflected as the XRD peak shifting in the present case.

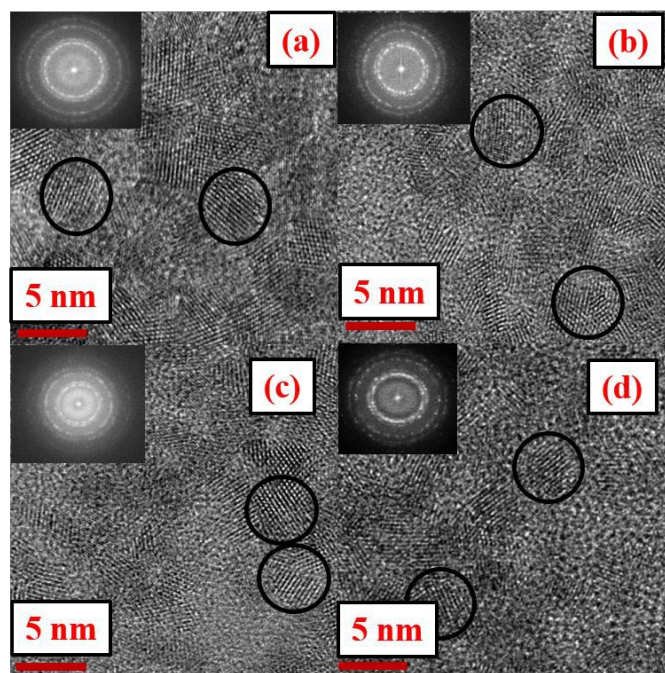


Fig.2 (Colour online) TEM images of (a) CeO₂ NPs, (b) Ce_{0.9}Eu_{0.1}O₂ NPs, (c) Ce_{0.8}Eu_{0.2}O₂ NPs and (d) Ce_{0.7}Eu_{0.3}O₂ NPs, respectively. Insets in the each figure show the SAED patterns of respective sample.

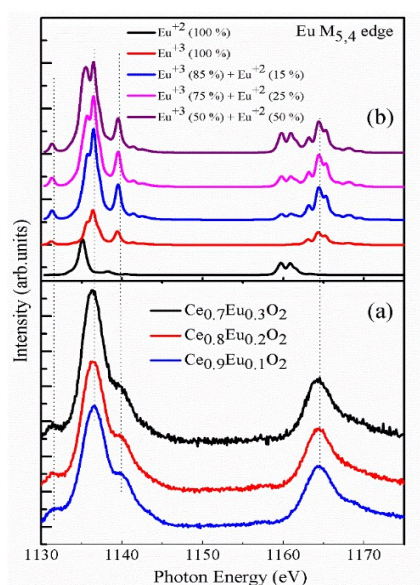


Fig. 3 (Colour online) (a) Eu M_{5,4}-edge spectra of Ce_{1-x}Eu_xO₂ (x = 0.1 - 0.3) NPs. (b) simulated Ce M_{5,4}-edge spectra for the +2 and +3 valance state of Eu by using atomic-multiplet calculation. Different combinations, with different weight percentage of spectra, of the theoretical Eu⁺³ and Eu⁺² M_{5,4}-edge are produced to fairly match with the experimental data.

To further confirm the size and morphology of the NPs, systematic, HR-TEM measurement was performed on the samples. Fig. 2 (a-d) shows the TEM images of pure CeO₂, Ce_{0.9}Eu_{0.1}O₂, Ce_{0.8}Eu_{0.2}O₂, and Ce_{0.7}Eu_{0.3}O₂ samples, respectively. The SAED pattern of each sample is also provided in the inset of each TEM image. It is clear from the Fig.2 that all the samples show the spherical kind of morphology with the average diameter of ~ 5±0.5 nm. The encircled area in the TEM images shows the view of the particles and crystallographic planes. The ring patterns in the SAED images are conveying the polycrystalline nature of all the samples, and they support the findings of XRD measurements. Though marginal agglomeration of NPs is present in all of the samples, such agglomeration is anticipated in the chemical precipitation method grown NPs due to the presence of hydroxyl ions on the surface of NPs^{19, 22}. Our structural investigations ruled out the formation of secondary phases, convincing the substitutional doping of Eu ions at the Ce sites in CeO₂ lattice up to x = 0.3; however, the local atomic disorder/structural perturbations were also observed (XRD peak broadening and decrease in the peak intensity). Such structural perturbations are expected to facilitate the interesting variations in electronic structure properties of CeO₂:Eu NPs and shall be discussed in the following sections.

XANES study at the Eu M_{5,4} -edge, O K-edge, Ce M_{5,4} -edge, Ce K-edge and Eu L-edge

To verify the valence state of Eu in CeO₂ lattice, the Eu M_{5,4}-edge spectra were studied. Fig. 3 (a) shows the Eu M_{5,4}-edge spectra of Ce_{1-x}Eu_xO₂ (x = 0.1 to 0.3) samples. The favourable valence state of Eu ions is +3, however, +2 valence state of Eu has also been reported when the Eu doping concentrations were large²³. Therefore, to clear these doubt, we have employed atomic-multiplet calculations to

ARTICLE

PCCP

generate theoretical Eu $M_{5,4}$ edge spectra from the Eu^{+2} and Eu^{+3} ions and presented in the Fig. 3 (b). To compare the discrete lines of the atomic-multiplets with the experiment and to simulate the resolution, they have been broadened with the Lorentzian width of 0.08 eV and Gaussian width of 0.2 eV. Various combinations, with different weight percentage of spectra, of the theoretical Eu^{+3} and Eu^{+2} $M_{5,4}$ -edge were generated. The atomic-multiplet calculations show that the experimental Eu $M_{5,4}$ edges spectra, from all of the samples, were fairly resembled to those of theoretical Eu^{+3} $M_{5,4}$ -edge and, hence, they suggest the presence of +3 valence state of Eu ions in the doped CeO_2 NPs. It is noticeable from the Fig. 3 (a) that the intensity of experimental XANES data at Eu M_5 and M_4 edges is enhanced with increasing the Eu concentration. This indicates the improvement in the hybridization strength of Eu d and f orbitals with the doping concentration.

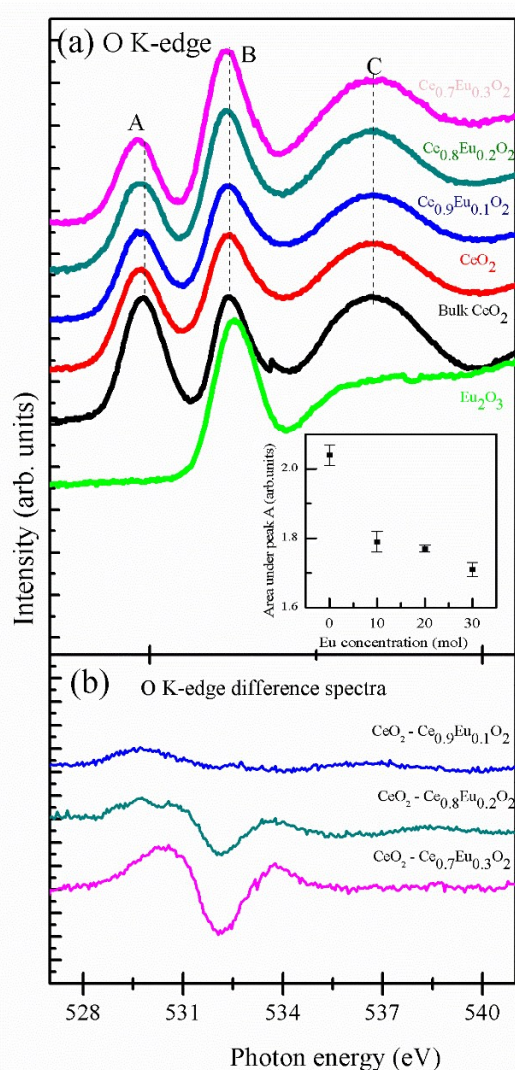


Fig. 4. (Colour online) (a) O K-edge spectra of $\text{Ce}_{1-x}\text{Eu}_x\text{O}_2$ ($x=0.0-0.3$) NPs along with the spectra of bulk CeO_2 and Eu_2O_3 . (b) Difference spectra, obtained by subtracting the O K-edge spectra of Eu doped nanoparticle samples from the spectrum of undoped CeO_2 nanoparticle sample. Inset shows the variation in the area under the pre-edge peak (A) as a function of Eu concentrations. The spectra are vertically shifted for the clarity of data.

Fig. 4 (a) shows the normalized XANES spectra at the O K-edge of $\text{Ce}_{1-x}\text{Eu}_x\text{O}_2$ ($x = 0.0$ to 0.3) NPs along with the bulk CeO_2 and Eu_2O_3 samples. It can be seen from the Fig. 4 (a) that O K-edge spectra of bulk CeO_2 and $\text{Ce}_{1-x}\text{Eu}_x\text{O}_2$ ($x = 0.0$ to 0.3) NPs show three intense peaks (A, B and C) at 530.0 eV, 532.5 eV and 536.9 eV. These features can be assigned to the hybridization of the empty O $2p$ states with the Ce $4f$, $5d_{e_g}$ and $5d_{t_{2g}}$ states, respectively^{19, 24}. The spectral profile of $\text{Ce}_{1-x}\text{Eu}_x\text{O}_2$ ($x = 0.0$ to 0.3) nanoparticle samples are closely resembled to those of bulk CeO_2 , except the peak broadening and intensity variation. The spectral features and peak positions in the O K-edge spectra of $\text{Ce}_{1-x}\text{Eu}_x\text{O}_2$ ($x = 0.0$ to 0.3) nanoparticle samples are different from spectral features of europium oxide, which indicates negligible presence of europium oxide phases. The crystal-field splitting energy (i.e., separation of e_g and t_{2g} features) is known to exceed, a bit, in the smaller sized NPs²⁴ (because of the association of larger surface with the smaller sized particles) and also varies with the hybridization strength of the d or f orbitals, with the O $2p$ orbitals, of the additive atoms¹⁹. Therefore, it gives information of the particle size and doping effects on the electronic structure properties of the host material. In the present case the crystal field effects are less discriminable in the pure and doped NPs because of the broadening of peak C.

While comparing the spectral features of Eu doped NPs samples relative to the undoped CeO_2 NPs, it seems that intensity of A peak is decreased and the intensity of B peak is increased. To understand this intensity variation, the difference spectra were obtained by subtracting the O K-edge spectra of Eu doped nanoparticle samples from the spectrum of undoped CeO_2 nanoparticle sample. It is visible from Fig. 4 (b) that the difference of peak ~ 530 eV (pre-edge peak) is increased in upward direction and the difference of peak ~ 532.5 ($5d_{e_g}$ peak) eV is enhanced in downward direction with the variation of Eu content. This indicates that the Eu doping has caused a net reduction in the Ce $4f$ unoccupied state and enhanced the density of empty d (e_g) states. It is also noticeable from the Fig 4 (b) that the peak at ~ 530 eV is splitted/broadened and the weight changes with Eu concentration. This may be because of the distortion in oxygen octahedra by Eu doping induced structural disorders via formation of $\text{Ce}^{+4}-\text{O}-\text{Eu}^{+3}$ and $\text{Ce}^{+3}-\text{O}-\text{Eu}^{+3}$ networks. The increase in the weight of spectral feature at ~ 530 eV (main notice in the spectral change) could be due to the net reduction of Ce $4f$ unoccupied states, hybridized with the O $2p$ states, with increasing the Eu contents. The enhancement in the available d states may be due to the mix-up of Eu related empty d states with the Ce d states in the $\text{Ce}_{1-x}\text{Eu}_x\text{O}_2$ ($x = 0.0$ to 0.3) compounds. The variation in the intensity of peak A implies a change in the hybridization of O $2p$ and Ce $4f$ states and reflects the change in the $4f$ occupancy number and the valence of Ce²⁴. To quantify the variation in the intensity of peak A, area under the curves was inspected by Gaussian peak fitting and presented in the inset of Fig. 4 (a). It is clearly visible that the area under the peak A is significantly decreased with Eu doping. The net decrease in the area under the peak A indicates that the Ce $4f$ orbitals are partially filled by the electrons or Ce^{+3} ions are formed via formation of oxygen ion vacancies in the Eu doped NPs. It is noticeable from the inset that

the decrease in the area under the peak A is substantial in case of $\text{Ce}_{0.9}\text{Eu}_{0.1}\text{O}_2$ NPs samples and then marginally decreased for the $\text{Ce}_{0.8}\text{Eu}_{0.2}\text{O}_2$ and $\text{Ce}_{0.7}\text{Eu}_{0.3}\text{O}_2$ NPs samples. Formation of $\text{Eu}^{+3} - \text{O} - \text{Ce}^{+4}$ and $\text{Eu}^{+3} - \text{O} - \text{Ce}^{+3}$ networks and decrease in the area under the pre-edge peak will be discussed in the following sections.

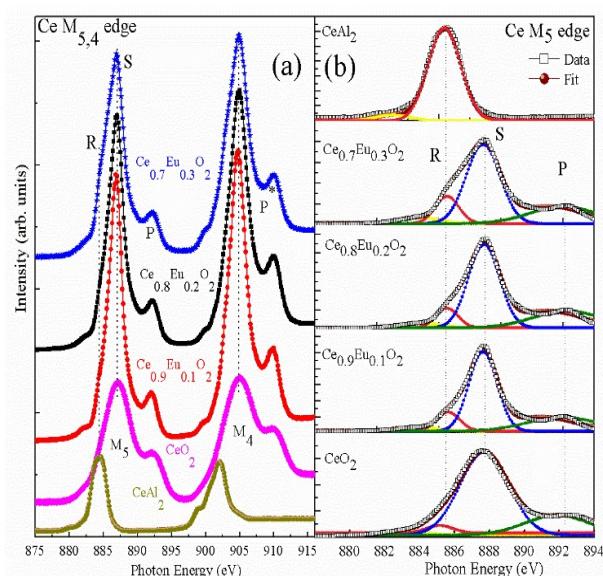


Fig. 5. (Colour online) (a) Ce M_{5,4}-edge spectra of $\text{Ce}_{1-x}\text{Eu}_x\text{O}_2$ ($x=0.0-0.3$) NPs along with the spectra of bulk CeAl_2 sample. (b) De-convolution of Ce M₅-edge spectra.

The Ce M_{5,4}-edge is attributed to the Ce 3d_{3/2} and 3d_{5/2} core level transitions into 4f unoccupied electronic state, and thus, directly reflects the occupancy of the 4f orbitals^{19,24}. To probe the variation in the valence state of Ce with Eu doping, systematic, XANES spectra at the Ce M_{5,4}-edge were collected and are shown in the Fig. 5 (a). To distinct the Ce valance state (+3 or +4), Ce M_{5,4}-edge XANES spectrum of CeAl_2 was also collected (Ce is regarded as trivalent and tetravalent in CeAl_2 and CeO_2 , respectively^{19,24}) and presented along with the spectra of $\text{Ce}_{1-x}\text{Eu}_x\text{O}_2$ ($x = 0.0$ to 0.3) NPs. It is visible from Fig. 5 (a) that all $\text{Ce}_{1-x}\text{Eu}_x\text{O}_2$ ($x = 0.0$ to 0.3) NPs show two major peaks at ~ 887 eV and at ~ 905 eV, representing the Ce M₅-edge and Ce M₄-edge, respectively. Besides, of these two major peaks, all of the as-synthesized samples show two post edge peaks at ~ 892 eV and at ~ 909.8 eV. The post-edge peaks are known to represent the contribution of 4f states because they originate from the transitions to the 4f states in the conduction band²⁵. At the first sight, the as-synthesized NPs are seemed to enclose both Ce^{+4} and Ce^{+3} ions, because the spectral features of $\text{Ce}_{1-x}\text{Eu}_x\text{O}_2$ ($x = 0.0$ to 0.3) NPs partially matches with spectral features of bulk CeAl_2 . The Ce M₄-edge is known as the replica of Ce M₅-edge. In order to understand the 3d transitions into 4f states and to reveal the variation in the valance state of Ce with Eu doping, the Ce M₅-edge was de-convoluted with its post edge peak P (using the Gaussian peak fittings) and the result is presented in Fig. 5(b). It is noticeable from the Fig. 5 (b) that the peak R evolves in the Eu doped CeO_2 NPs and

its intensity increases with increasing the Eu concentration, implying an increase in the Ce^{+3} contribution in Eu doped NPs. $\text{Ce}^{+3}/\text{Ce}^{+3}+\text{Ce}^{+4}$ ratio was calculated by examining the area under the R, S and P peaks, as a function of Eu concentration, and presented in the Fig. 6. The ratio of R to (S+P) is low, but non-zero, in the pure CeO_2 NPs implying that the Ce^{+4} is dominating in this sample with marginal presence of Ce^{+3} . R to (S+P) ratio is increased with increasing the Eu concentration, indicating that the Ce^{+4} is reduced to Ce^{+3} in the Eu doped samples. This variation in the $\text{Ce}^{+3}/\text{Ce}^{+3}+\text{Ce}^{+4}$ ratio tallies with the findings of the O K-edge results, where a net reduction in the unoccupied Ce 4f states was observed when Eu concentration was increased. It is noticeable that net decrease in the intensity of peak A in the O K-edge spectra and the increase in the $\text{Ce}^{+3}/\text{Ce}^{+3}+\text{Ce}^{+4}$ ratio are significant for the first 10 mol% Eu doping, indicating an efficient substitution of Ce^{+4} ions by the Eu^{+3} ions in the CeO_2 lattice and formation of favourable $\text{Ce}^{+4} - \text{O} - \text{Eu}^{+3}$ networks. At higher doping level, although $\text{Ce}^{+3}/\text{Ce}^{+3}+\text{Ce}^{+4}$ ratio increases and the area under the peak A of O K-edge decreases, some of the existing Ce^{+3} ions are expected to be substituted by the Eu^{+3} ions and form $\text{Ce}^{+3} - \text{O} - \text{Eu}^{+3}$ networks along with the $\text{Ce}^{+4} - \text{O} - \text{Eu}^{+3}$ networks. As a consequence of this, the increase in $\text{Ce}^{+3}/\text{Ce}^{+3}+\text{Ce}^{+4}$ ratio and decrease in the area under peak A of O K-edge spectra are complementary.

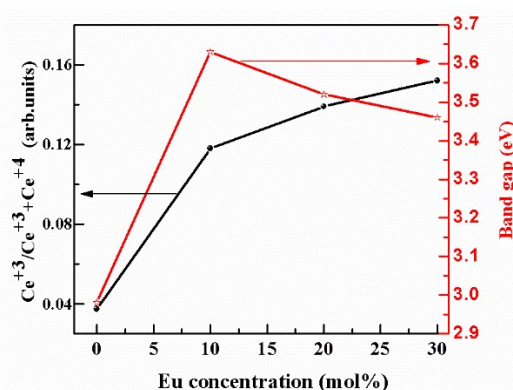


Fig. 6. $\text{Ce}^{+3}/\text{Ce}^{+3}+\text{Ce}^{+4}$ ratio, calculated from the de-convolution of Ce M₅-edge, as a function of Eu concentration.

To corroborate the results of Eu M_{5,4}-edge and Ce M_{5,4}-edge XANES and to get more insight about the valence state of metal ions in the as synthesized samples, we measured the Ce K-edge and Eu L-edge XANES spectra and presented in Fig. 7 (a-b). In the Fig. 7(a), the spectral features and white line position of Ce K-edge XANES are closely resembled to that of previously reported nanocrystalline ceria²⁶ and thus strengthened the formation of CeO_2 nanoparticle samples in the present study. It is clear from the Fig. 7 (a) that there is energy shift towards the lower energy in the Ce K-edge spectra for the Eu doped samples. The low energy shift signifies the partial reduction of cerium to its trivalent state²⁶. The energy shift (~ 2 eV) is dominant in the low concentration (10 mol%) Eu doped samples and then marginally varies for the higher Eu concentration doped CeO_2 . This implies that majority of Ce^{+4} ions have been reduced into Ce^{+3} ions within the low Eu doping concentration; however, a marginal reduction of Ce^{+4} into Ce^{+3} could take place by the further increase in the Eu content. This behaviour is consistent with the findings of Ce M_{5,4}-edge and support our assumption on the

ARTICLE

PCCP

substitution of a large number of Ce^{4+} ions by the Eu^{3+} ions in the CeO_2 lattice at the low Eu doping level; however, the replacement of Ce^{3+} ions by the Eu^{3+} is also likely at higher Eu doping. Therefore, low energy shift in the Ce K-edge spectra and calculated $\text{Ce}^{3+}/\text{Ce}^{3+}+\text{Ce}^{4+}$ ratio are in accordance with each other. Fig. 7 (b) shows the Eu L_{3-} edge XANES spectra of Eu doped CeO_2 samples. The spectral features from all of the samples are very similar to each other and resemble to the previously reported XANES spectra²⁷ for Eu^{3+} . In the spectra, we could not find any low energy peak related to the Eu^{2+} as observed by *Rakovan et al.* Thus the present Eu L-edge XANES tally our findings of the Eu $M_{5,4}$ -edge XANES that Eu^{3+} ions are present throughout the doping range. Increase in the intensity of Eu L-edge white line peak, which originates from the transitions from 2p to 5d states, indicates the net increase in the unoccupied states with Eu doping concentration. This behaviour could be attributed to the fair localization of Eu^{3+} ions within the CeO_2 lattice via formation of either $\text{Ce}^{4+}-\text{O}-\text{Eu}^{3+}$ or $\text{Ce}^{3+}-\text{O}-\text{Eu}^{3+}$ networks.

EXAFS study at Ce K-edge

EXAFS provides element specific and local short-range structural information, which is complementary to that provided by the XRD, and also includes information about the identification of the atoms surrounding the absorbing atom, coordination number and bond length etc.^{19, 23-24}. In a typical EXAFS spectrum, the plot of absorption ($\mu(E)$) versus photon energy (eV) is obtained by monitoring the intensities I_0 and I_t . In determining the I_t , thickness (t) and absorption coefficient (μ) of the sample material play crucial role, given by the relation: $I_t = I_0 e^{-\mu t}$. The absorption function is achieved from the absorption coefficient by using the relation²⁸:

$$\chi(E) = \frac{\mu(E) - \mu_0(E)}{\Delta\mu_0(E_0)}$$

where, $\mu_0(E_0)$ is the bare atom background,

$\Delta\mu_0(E_0)$ is the step in the $\mu(E)$ value at the absorption edge and the E_0 is the absorption edge energy. During the analysis of data, the EXAFS function was derived from the raw absorption data through pre-edge and post-edge background subtraction and then normalization with respect to the edge jump by using the *ATHENA* software package²⁹. After being k^3 -weighted, k is the photo-electron wavenumber given by $k = \left[\frac{2m(E - E_0)}{\hbar^2} \right]^{1/2}$, the EXAFS function was Fourier

transformed from k -space to r -space to generate the $\chi(R)$ versus R (or FT-EXAFS) spectra in terms of the real distance from the central absorbing atom. To simulate the FT-EXAFS data, theoretical CeO_2 structure (space group- $Fm\bar{3}m$, $a = b = c = 5.410 \text{ \AA}$, $\alpha = \beta = \gamma = 90^\circ$) was generated using the ARTIMIS (ATOM and FEFF codes) software package³⁰. The data range taken for the transformation was $2\text{--}10 \text{ \AA}^{-1}$ in the k -space. Structural parameters were obtained, without phase corrections, by fitting the data in the r -space within the interval of $1\text{--}6 \text{ \AA}$. Fig 8 show the $\chi(R)$ vs. R spectra along with the corresponding best fit theoretical spectra of pure and Eu doped CeO_2 NPs. Structural parameters obtained from the Ce K-edge EXAFS fittings are tabulated in the Table1. The first and the second shells in the CeO_2 K-edge EXAFS data arise from the single scattering paths of Ce–O and Ce–Ce paths, respectively^{19, 24}.

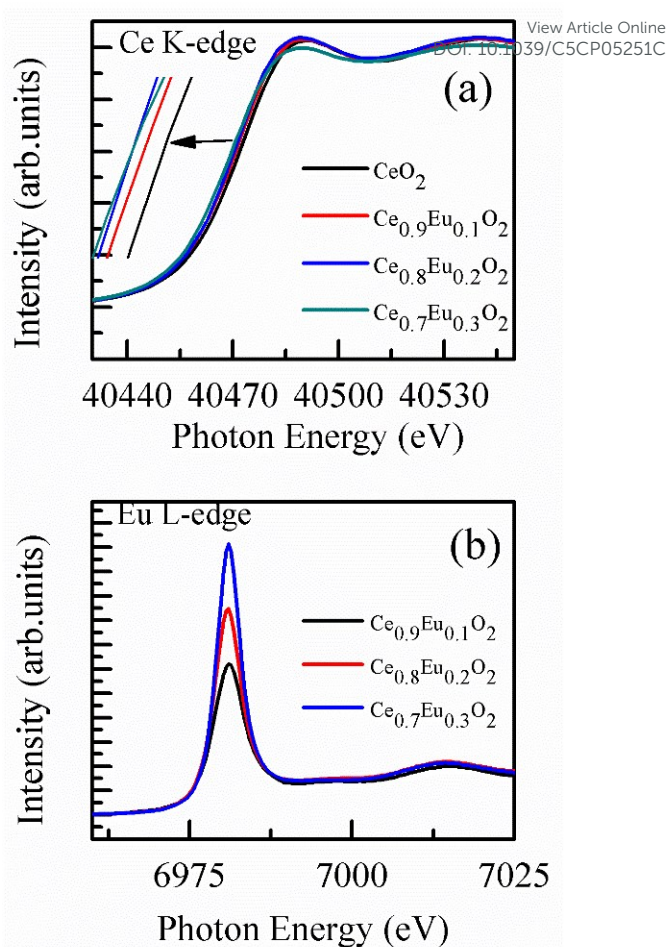


Fig. 7. (Colour online) (a) Ce K-edge XANES spectra of $\text{Ce}_{1-x}\text{Eu}_x\text{O}_2$ ($x=0.0-0.3$) NPs. (b) Eu L_{3-} edge XANES spectra of $\text{Ce}_{1-x}\text{Eu}_x\text{O}_2$ ($x=0.1-0.3$) NPs.

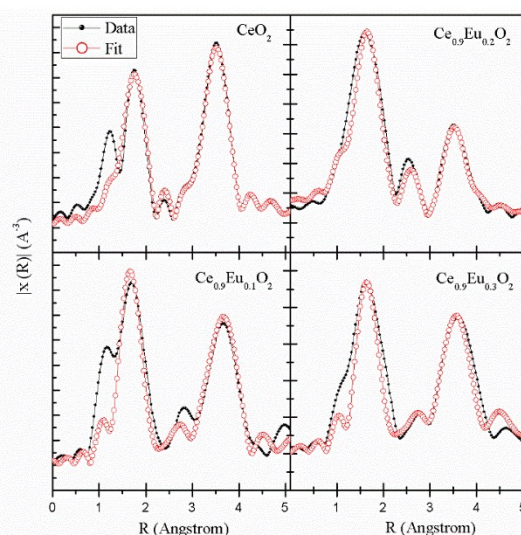


Fig. 8. (Colour online) Radial distribution function [$\chi(R)$ vs. R] spectra along with the theoretical fits for $\text{Ce}_{1-x}\text{Eu}_x\text{O}_2$ ($x=0.0-0.3$) NPs.

The third and the fourth peaks contain single and multiple scattering contributions from a variety of paths, such as O – Ce – O, Ce – O – Ce, etc. Therefore, larger uncertainties in the third/fourth shell fitted parameters have been observed in the derived parameters³¹. In the present study, we focussed on the fittings of Ce – O and Ce – Ce paths for undoped CeO₂ and Ce – O, Ce – Ce and Ce – Eu paths for Eu doped CeO₂ samples. The first peak in the Fig. 8 at ~ 1.65 Å is assigned to the Ce – O shell and the second peak ~ 3.58 Å is assigned to the Ce – Ce shell of CeO₂ compound. The third Ce – O shell seems to overlap with the second Ce – Ce or Ce – Eu shell and is consistent to the previous reports because of the closer radial distribution functions of these two shells^{24,31}. It is clear from the Fig. 8 that CeO₂ theoretical structure was fairly generated for all of the samples and nullify the peaks from the Eu-oxide or metallic Eu/Ce, indicating the single phase formation of Eu-doped CeO₂ NPs in the present study and supporting the XRD results. It is noticeable from the table 1 that O coordination number and bond distance are decreased in the whole range of Eu doping. In general, the oxygen coordination is high (8) in the bulk CeO₂³¹ because of octahedral environment (O_h) of oxygen atoms within the ceria lattice. In the present case, the oxygen coordination number is found to lower, even, in the pure CeO₂ NPs. This may be due the fact that larger number of atoms reside on the surface of nano-dimensional samples and V_o^{--} are generated in the small and/or doped oxide NPs^{13,25}. It is also observed that bond length of Ce – Ce shell is enlarged with 10 mol% Eu doping and then slightly decreased for the higher Eu doping. This indicates that at the lower Eu doping the Eu³⁺ ions are expected to replace the Ce⁴⁺ ions (ionic radii of Eu³⁺ > Ce⁴⁺) in the CeO₂ lattice resulting an enlargement in Ce – Ce shell via formation of Ce⁴⁺ – O – Eu³⁺ networks. Further increase in the Eu³⁺ doping may leads to formation of Ce³⁺ – O – Eu³⁺ networks (ionic radii of Eu³⁺ \sim Ce³⁺) along with the Ce⁴⁺ – O – Eu³⁺ networks. Thus, the existence of both networks may affect the Ce – Ce shell at the higher Eu doping.

Table 1. Structural parameters obtained from the Ce K-edge EXAFS fittings (bond distance (R), coordination number (N), Debye-Waller (DW) factor, edge-energy correlation (ΔE) and r-factor).

Sample name	Shell	R	CN	DW factor	ΔE (eV)	r-factor
CeO ₂	Ce – O	2.33(77)	7.8	0.008(2)	-4.9	0.075
	Ce – Ce	3.84(60)	11.8	0.007(3)		
Ce _{0.9} Eu _{0.1} O ₂	Ce – O	2.29(10)	6.5	0.005(6)	-5.2	0.321
	Ce – Eu	3.83(50)	3.1	0.019(1)		
	Ce – Ce	3.85(64)	7.3	0.005(1)		
Ce _{0.8} Eu _{0.2} O ₂	Ce – O	2.28(38)	6.4	0.007(7)	-5.2	0.142
	Ce – Eu	3.81(46)	3.6	0.009(4)		
	Ce – Ce	3.84(53)	7.1	0.005(1)		
Ce _{0.7} Eu _{0.3} O ₂	Ce – O	2.26(06)	6.4	0.006(7)	-4.8	0.478
	Ce – Eu	3.80(54)	4.0	0.009(1)		
	Ce – Ce	3.84(64)	6.7	0.008(1)		

UV-visible absorption spectroscopy study

UV-visible absorption spectroscopy is known to probe size-confinement effects in the NPs and provides information on defect sites in the materials^{13,16}. Therefore, in order to understand the grain-size variation and doping effects on the optical absorption and

band gap of the as-synthesized samples, systematic UV-visible absorption spectroscopy measurements were conducted on Ce_{1-x}Eu_xO₂ ($x = 0.0$ to 0.3) NPs and the results are shown in the Fig. 9. It is noticeable from the spectra that the absorption edge shows variations with the Eu doping. The band gap energy was calculated by plotting the $(\alpha h\nu)^2$ versus photon energy ($h\nu$) for each sample, as shown in the inset of the Fig. 9. The intersection of the extrapolated linear portions gives the direct band gap energy^{13,16}. Thus calculated band gap energy of Ce_{1-x}Eu_xO₂ ($x = 0.0$ to 0.3) NPs is 2.98 eV, 3.63 eV, 3.52 eV and 3.46 eV, respectively, and presented in the Fig. 6. It is evidenced from the Fig. 6 that the 10 mol% Eu doping not only enhanced the band gap energy but also increased Ce³⁺ concentration in the CeO₂ host. Particle size reduction was expected to increase the band gap energy. But, in contrary to this, we observed a marginal increase in the Ce³⁺/Ce⁴⁺+Ce³⁺ ratio and little decrease in the band gap energy in the higher Eu content doped CeO₂ NPs samples. The increase in the band gap energy and blue shift in the absorption edge arise not only by the particle size reduction but also due to the reduction of the valence state of Ce⁴⁺ ions into Ce³⁺ ions³². The net reduction of Ce⁴⁺ into Ce³⁺ ions increases the charge transfer gap between the O 2p and Ce 4f bands and results in the blue shift in the absorption spectrum of CeO₂ NPs^{13,32}. At low doping concentration (10 mol%) most of the Eu³⁺ dopant are expected to replace the Ce⁴⁺ ions in the CeO₂ lattice via formation of Ce⁴⁺ – O – Eu³⁺ networks which gives a plenty of O vacancies and thus more Ce³⁺ ions in the CeO₂ host. With increasing the Eu contents some of the Ce³⁺ sites can be occupied by Eu³⁺ ions and the formation of, both, Ce⁴⁺ – O – Eu³⁺ and Ce³⁺ – O – Eu³⁺ networks may lower the band gap energy, by narrowing the charge-transfer gap between O 2p and Ce 4f bands, and also resulting in marginal increase in Ce³⁺/Ce⁴⁺+Ce³⁺ ratio. Hence, our UV-visible absorption spectra helps us to understand that the particle size reduction is not only the factor to engineer the optical band gap but the Eu doping induced structural/electronic structure perturbations also play an important role.

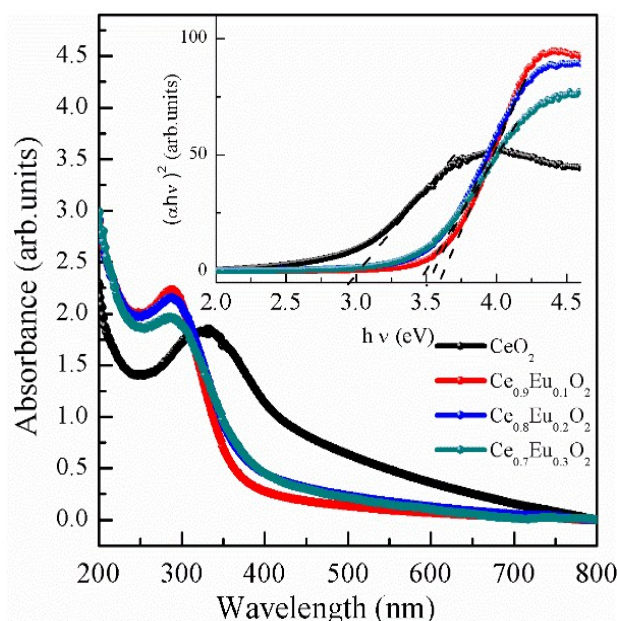


Fig. 9. (Colour online) UV-visible absorption spectra of Ce_{1-x}Eu_xO₂ ($x=0.0$ – 0.3) NPs. Inset shows the band gap energy determination by plotting the $(\alpha h\nu)^2$ versus photon energy ($h\nu$) curves for each sample.

ARTICLE

PCCP

Photoluminescence study

To probe the luminescence property of as synthesized samples, excitation and emission spectra of $\text{Ce}_{1-x}\text{Eu}_x\text{O}_2$ ($x = 0.0$ to 0.3) NPs were recorded. The excitation spectra are collected by measuring the emission intensity at a fixed wavelength (615 nm). It is visible from the Fig. 10 (a) that pure CeO_2 does not exhibit any excitation peak throughout the wavelength range escape of one band at 309 nm; whereas, the $\text{Ce}_{1-x}\text{Eu}_x\text{O}_2$ ($x = 0.1$ to 0.3) NPs have shown three major spectral features at 393 nm, 414 nm and 463 nm. In the previous reports, the $\text{CeO}_2\text{:Eu}$ NPs have shown a broad band between 300 – 350 nm which originates from the charge transfer (CT) transitions between O^{2-} and Ce^{4+} ions of the CeO_2 host¹⁵. In the present case, the peak at 309 nm is not broaden enough; however, its position lies within the range of CT transitions of CeO_2 host. The sharp peaks at 393 nm, 414 nm and 463 nm can be assigned to the intra-configurational $4f-4f$ transition of Eu^{3+} in the CeO_2 lattice: 7F_0 to 5L_6 , 5D_3 , and 5D_2 , etc.¹⁴⁻¹⁵. In the excitation spectra, the dominant excitation peak is at 463 nm which is corresponding to $7\text{F}_0 - 5\text{D}_2$ transition¹⁵. This peak position fairly matches with the emission of commercial GaN light emitting diodes (440–470 nm) chips. Further, the appearance of 463 nm peak in the present excitation spectra is quite different from the other Eu^{3+} activated molybdates and tungstates samples which exhibit the strongest excitation line at 395 nm in the near-UV-region¹⁵. It is also noticeable from the Fig. 10 (a) that the intensity of peaks at 393 nm, 414 nm and 463 nm increases with increasing the Eu concentration, while excited with blue light, indicating that the red phosphor materials having similar optical properties to that of commercial GaN light emitting diodes can be synthesized using the chemical precipitation method with varying Eu concentrations.

Fig. 10 (b) presents the emission spectra of $\text{Ce}_{1-x}\text{Eu}_x\text{O}_2$ ($x = 0.0$ to 0.3) NPs collected under the excitation wavelength of 466 nm. It is visible from the emission spectra that the pure CeO_2 does not exhibit any emission peak under the excitation of 466 nm light wavelength; whereas the $\text{Ce}_{1-x}\text{Eu}_x\text{O}_2$ ($x = 0.1$ to 0.3) NPs exhibit several emission peaks between orange-to-red region of the solar spectrum (at 593 nm, 617 nm, 628 nm, 654 nm and 702 nm). The multiple emission peaks in the present spectra are due to the splitting of Eu^{3+} $4f$ shells and mainly originate from the combination of magnetic dipole (MD) and electric dipole (ED) transitions^{14-16, 33}. The MD and ED transitions are very specific to the environment of Eu^{3+} ions in the host material. The MD transition ($5\text{D}_0 - 7\text{F}_1$, around 590–600 nm) usually dominates when the Eu^{3+} ions occupy the lattice sites with inversion centers. However, if the Eu^{3+} ions are located in the sites of without centrosymmetry, the ED transition ($5\text{D}_0 - 7\text{F}_2$, around the 610–630 nm) plays a crucial role^{14, 33}. In the present emission spectra the peak at 593 nm is assigned to MD ($5\text{D}_0 - 7\text{F}_1$) transition and the peaks at 617 nm, 628 nm are due to ED ($5\text{D}_0 - 7\text{F}_2$) transitions and rest of the peaks are due to the upper splitting transitions of Eu $4f$ shells. Our XRD results have confirmed the single phase formation of CeO_2 NPs with space group of $\text{Fm}\bar{3}\text{m}$; within the CeO_2 lattice the point-group symmetry of Ce sites is ideally O_h ; i.e., every Ce ion is surrounded by eight equatorial oxygen ions.

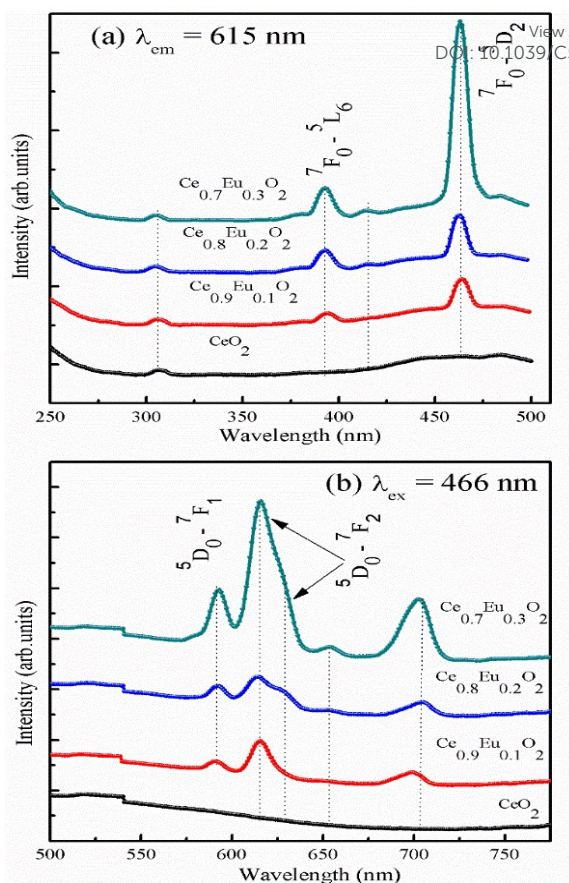


Fig. 10. (Colour online) (a) Excitation spectra of $\text{Ce}_{1-x}\text{Eu}_x\text{O}_2$ ($x=0.0-0.3$) NPs for the emission wavelength of 615 nm. (b) Emission spectra of $\text{Ce}_{1-x}\text{Eu}_x\text{O}_2$ ($x=0.0-0.3$) NPs excited with wavelength of 466 nm.

When Eu substitutes the Ce in CeO_2 lattice the O_h symmetry can be either improved or lowered, depending on the site occupancy of Eu^{3+} ions. Since the Ce can exist in Ce^{4+} and Ce^{3+} ionic states in CeO_2 NPs, doping of Eu^{3+} ions may form $\text{Ce}^{4+}-\text{O}-\text{Eu}^{3+}$ or $\text{Ce}^{3+}-\text{O}-\text{Eu}^{3+}$ networks. It is also known that the size of Eu^{3+} ions is larger than that of Ce^{4+} ions and comparable to that of Ce^{3+} ions, which gives lower symmetric $\text{Ce}^{4+}-\text{O}-\text{Eu}^{3+}$ and higher symmetric of $\text{Eu}^{3+}-\text{O}-\text{Ce}^{3+}$ networks in the Eu doped CeO_2 NPs.

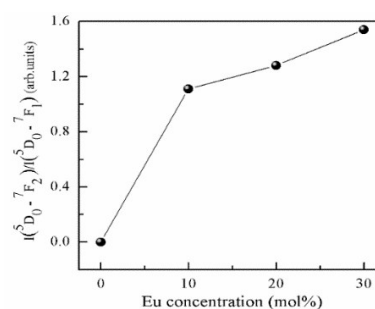


Fig. 11. Intensity ratio of $5\text{D}_0 - 7\text{F}_2$ and $5\text{D}_0 - 7\text{F}_1$ transitions as a function of Eu concentration.

In the present case the MD and ED transitions (peaks at 593 nm and 617 nm, respectively) were appeared within the lowest doping concentration of Eu, indicating the fruition of PL properties in the host CeO_2 without losing the FCC lattice. Similar to the previous reports²³, on the PL properties of other trivalent dopants (i.e., Dy^{+3} and Sm^{+3}) in CeO_2 systems, the intensity of all the emission peaks, in the present study, also improved with increasing the Eu concentration. The apparent changes in the emission spectra are the enhancement in the intensity of MD and ED transitions and evolution of 628 nm peak, after the 20 mol.% Eu doping. It is known that, the intensity ratio of $^5\text{D}_0 - ^7\text{F}_2$ and $^5\text{D}_0 - ^7\text{F}_1$ transitions is called asymmetry ratio of the lattice and signifies the degree of distortion from the inversion symmetry of CeO_2 ^{14,33}. Fig. 11 shows that $I(^5\text{D}_0 - ^7\text{F}_2)/I(^5\text{D}_0 - ^7\text{F}_1)$ ratio increases for $\text{Ce}_{1-x}\text{Eu}_x\text{O}_2$ ($x = 0.0$ to 0.3) NPs, with increasing the Eu concentration, indicating that the Eu^{+3} ions mainly occupy those lattice sites (i.e., Ce^{+4} sites) which can reduce the O_h inversion symmetry of CeO_2 cell. Furthermore, noticeable increase in the MD transition has also been observed in the emission spectra with increasing the Eu concentration. This indicates that Eu^{+3} ions not only substitute the Ce^{+4} ions but also occupy the Ce^{+3} sites in the oxygen deficient CeO_2 lattice. Our O K-edge, Ce $\text{M}_{5,4}$ -edge and Ce K-edge XANES spectra have shown a net reduction of Ce^{+4} into Ce^{+3} with increase in the Eu concentration. However, the increase of Ce^{+3} is prominent in the 10 mol% Eu doped CeO_2 and then marginally increase for the higher Eu content doped samples. This could be possible if a fraction of Eu^{+3} ions occupy the Ce^{+3} sites (i.e., formation of $\text{Ce}^{+3} - \text{O} - \text{Eu}^{+3}$ networks) in case of the higher Eu concentration doped CeO_2 samples which favour MD transition induced PL properties along with ED transitions.

Photocatalyst study

Photocatalytic performances of the $\text{Ce}_{1-x}\text{Eu}_x\text{O}_2$ NPs were investigated by the degradation of MO aqueous solution under the UV light irradiation. Fig. 12 (a-e) show UV-visible spectra of MO aqueous solution, taken at different time intervals, in the absence and presence of catalyst samples. It is visible from the Fig. 12 (a) that the MO aqueous solution was hardly degraded, under the similar experimental conditions, when no catalyst was employed with the dye solution. When MO dye solutions were subjected to the as-synthesized $\text{Ce}_{1-x}\text{Eu}_x\text{O}_2$ NPs, under the light irradiation, the dye was degraded to different extents by each of the samples indicating specific photocatalytic properties of individual sample. The characteristic absorption peak of MO, at ~ 464 nm, was monitored to evaluate the photocatalyst performance of the samples. Fig. 13 shows the C_t/C_0 ratio of the catalyst samples, where C_0 is the initial intensity of absorption peak, recorded in the dark, and C_t is the intensity of same absorption peak at the different time of light irradiation. It is noticeable from the Fig. 13 that catalyst performance enhances with increasing the Eu concentration. It has been reported that the catalyst properties of the catalyst materials depends on their size, morphology and electronic structure properties³⁴⁻³⁷. In the present case, we could not observe any special morphology (i.e., rod, wire or other fascinating structures) in the TEM results escape of some spherical NPs in all of the samples. Therefore, the observed variations in the catalyst performance are expected to relate with the structural and electronic structural perturbations caused by the Eu doping in the CeO_2 lattice.

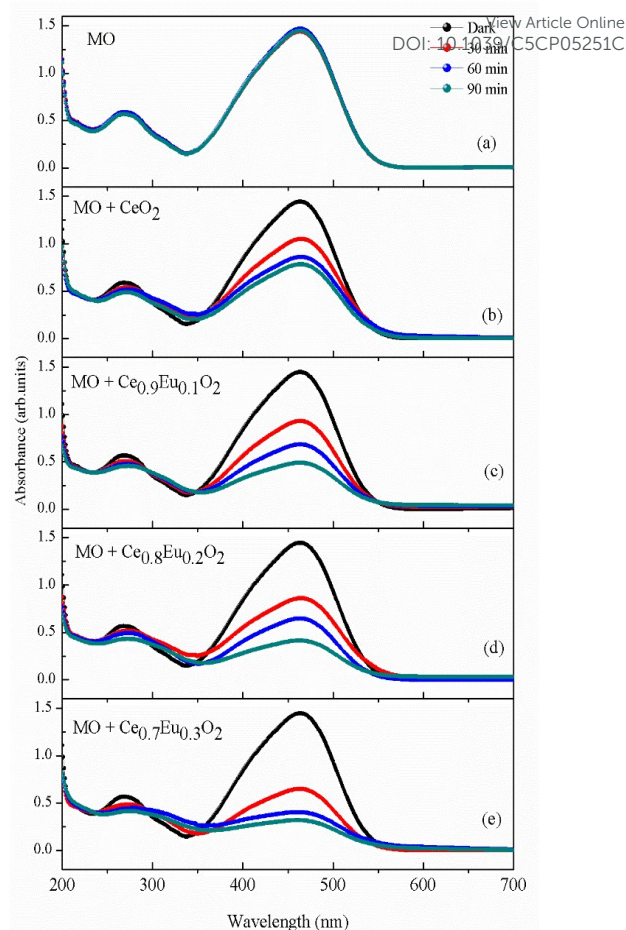


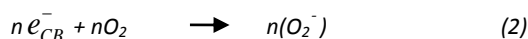
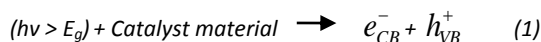
Fig. 12. (Colour online) UV-visible absorption spectra, taken at different time intervals of light irradiation, of (a) MO solution without catalyst, (b) MO solution with pure CeO_2 NPs, (c) MO solution with $\text{Ce}_{0.9}\text{Eu}_{0.1}\text{O}_2$ NPs, (d) MO solution with $\text{Ce}_{0.8}\text{Eu}_{0.2}\text{O}_2$ NPs and (e) MO solution with $\text{Ce}_{0.7}\text{Eu}_{0.3}\text{O}_2$ NPs.

An elemental insertion of Eu in the CeO_2 lattice may advance the electron density of the compound by altering the valance state of cations and oxygen concentration¹⁴⁻¹⁶ and this is evidenced by the O K-edge, Ce $\text{M}_{5,4}$ -edge and Ce K-edge XANES results in the present study. The large number of photo generated $e^- - h^+$ pairs are also essential to establish the oxidation-reduction reactions for degrading the azo dye^{18,35-36}. In the present case, although the energy band gap was found to increase in the Eu doped NPs, the energy of photons, provided by the mercury light source, is quite enough to generate large number of $e^- - h^+$ pairs from the electronic density advanced $\text{Ce}_{1-x}\text{Eu}_x\text{O}_2$ ($x = 0.0 - 0.3$) NPs. It is also inferred from the PL measurements that the enhanced electronic transition (excitation and de-excitation) takes place in the Eu doped samples which resulted in the excellent PL properties. Therefore, in the present photocatalyst study the Eu doping induced advance electronic density is expected to enhance the photocatalytic performance of higher Eu content doped CeO_2 NPs. Further, XRD results have shown a little size reduction for the Eu doped NPs. The smaller size provides larger surface area to the adsorption reactions of MO dye on to the NPs surface^{18,35-37}, and higher migration rates of photo-generated charge carriers, towards the surface, have also been observed in the case of smaller sized NPs³⁸. Photocatalytic activity of the luminescent NPs is presented in the schematic diagram (see Fig. 14). Here we expect that significant adsorption reactions have been taken

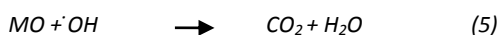
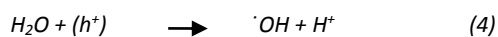
ARTICLE

PCCP

place on the small sized NPs (6.25 nm – 4.15 nm) and photo-generated $e^- - h^+$ pairs provide effective pathways for the oxidation (from the holes) and reduction (from the electrons) reactions to degrade the MO dye molecules. The photoelectrons scavenge the molecular oxygen and produce hydrogen-peroxide molecules in the aqueous medium^{18, 36} by the following reactions;



On the other hand, the holes generate hydroxyl radicals from the water¹⁸⁻³⁴. The hydroxyl radicals work as a powerful oxidizing agent and degrade most of the pollutant dyes^{18, 34-36} by the following reactions;



Therefore, the vigorous adsorption and redox reactions from the electronic structurally advanced Eu doped CeO_2 NPs are responsible for high catalyst performance of doped NPs.

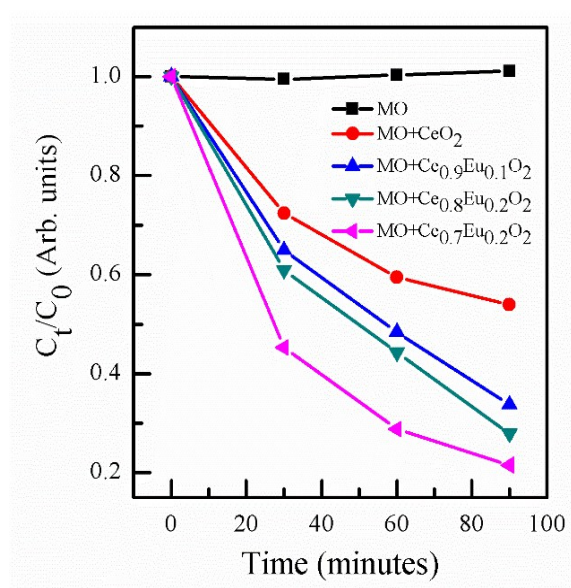


Fig. 13. (Colour online) Photocatalytic performance of catalyst samples by monitoring the absorbance of the 464 nm peak for degradation of MO at different time intervals of light irradiation.

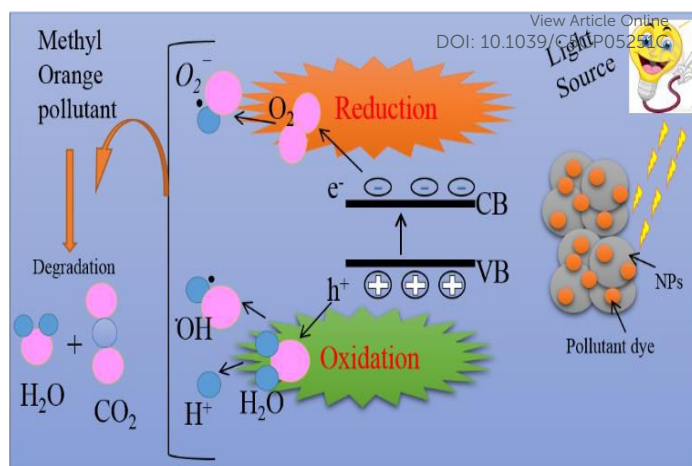


Fig. 14. (Colour online) Schematic of the generation of electron-hole pairs and the degradation of MO pollutant dye, via oxidation and reduction reactions.

Conclusions

Pure and Eu doped (up to 30 mol.%) CeO_2 NPs were synthesized using the chemical precipitation method. XRD and TEM results have shown formation of small (6.2 nm – 4.1 nm) sized and single phase NPs. Eu $M_{5,4}$ -edge and Eu L-edge XANES results have confirmed the existence of Eu^{+3} ions in the CeO_2 lattice within the entire doping range. Analysis of the O K-edge spectra, Ce M_{5} -edge spectra and Ce K-edge spectra show that Ce^{+4} ions reduce to Ce^{+3} ions via substitutional doping of Eu^{+3} ions in CeO_2 lattice. The substitutional doping of Eu in the CeO_2 lattice reduces the local O_h symmetry via creating oxygen vacancies/ Ce^{+3} ions and thus favors the ED transitions ($^5D_0 - ^7F_2$) induced optical emission in the CeO_2 . At higher Eu doping the $Ce^{+3} - O - Eu^{+3}$ networks also form along with $Ce^{+4} - O - Eu^{+3}$ networks and fertilize the MD ($^5D_0 - ^7F_1$) and ED transitions induced PL properties in the samples. Furthermore, enhanced photocatalytic performance of NPs indicates that Eu doping induced modified electronic structure of CeO_2 can offer its applicability in the photocatalyst applications.

Acknowledgements

Aditya Sharma, Mayora Varshney and Hyun-Joon Shin would like to acknowledge the financial support by the Basic Science Research Program (No. 2008-0062606, CELA-NCRC and NRF- 2015R1A5A1009962) through the National Research Foundation of Korea (NRF) and by the Converging Research Centre Program (2013K000306), funded by the Korea government Ministry of Science, ICT and Future Planning (MSIP). Authors are also thankful to Dr. Nam-Suk Lee (NINT-POSTECH), Dr. T. Jeon (3 D beam line of PAL) and Dr. M. G. Kim (10 C beam line of PAL) for their helps in the TEM, XRD, XANES/EXAFS measurements.

Notes and references

1. A. Corma, P. Atienzar, H. Garcia and J.Y.C. Ching, *Nat. Mat.*, 2004, 3, 394-397.
2. A. Sundaresan, and C.N.R. Rao, *Nano Today*, 2009, 4, 96-106.
3. W.C. Chueh, Y. Hao, W. C. Jung and S. M. Haile, *Nat. Mat.* 2012, 11, 155-161.
4. P. Chetri, B. Saikia, and A. Choudhury, *J. Appl. Phys.*, 2013, 113, 233514-233521.
5. L. Wang, H. Huang, S. Xiao, D. Cai, Y. Liu, B. Liu, D. Wang, C. Wang, H. Li, Y. Wang, Q. Li, and T. Wang, *ACS Appl. Mater. Interfaces*, 2014, 6, 14131-141140.
6. M. Shishkin and T. Ziegler, *J. Phys. Chem. C* 2010, 114, 21411-21416.
7. Y. Feng, L. Liu and X. Wang, *J. Mater. Chem.*, 2011, 21, 15442-15448.
8. X. Zhu, L. Yuan, G. Liang and A. Gu, *J. Mater. Chem. A*, 2014, 2, 11286-11298.
9. A.S. Karakoti, N.A. Monteiro-Riviere, R. Aggarwal, J.P. Davis, R.J. Narayan, W.T. Self, J. McGinnis, and S. Seal, *JOM*, 2008, 60, 33-37.
10. R. W. Tarnuzzer, J. Colon, S. Patil, and S. Seal, *Nano Lett.*, 2005, 5, 2573-2577.
11. M. Das, S. Patil, N. Bhargava, J. F. Kang, L. M. Riedel, S. Seal, and J. Hickman, *Biomaterials*, 2007, 28, 1918-1925.
12. Y. Xijuan, X. Pingbob and S. Qingde, *Phys. Chem. Chem. Phys.*, 2001, 3, 5266-5269.
13. Z. Wang, Z. Quan, and J. Lin, *Inorganic Chemistry*, 2007, 46, 5237-5242.
14. A. Kumar, S. Babu, A.S. Karakoti, A. Schulte and S. Seal, *Langmuir*, 2009, 25, 10998-11007.
15. S. Shi, M. Hossu, R. Hall and W. Chen, *J. Mat. Chem.*, 2012, 22, 23461-23467.
16. J. Roh, S. H. Hwang and J. Jang, *ACS Appl. Mater. Interfaces*, 2014, 6, 19825-19832.
17. G. Zhang, J. Ao, Y. Guo, Z. Zhang, M. Shao, L. Wang, L. Zhou and J. Shao, *RSC Adv.*, 2014, 4, 20131-20135.
18. A. Sharma, M. Varshney, J. H. Park, K. H. Chae, H. J. Shin, *RSC Adv.*, 5, (2015) 21762-21771.
19. A. Sharma, M. Varshney, H. J. Shin, Y. J. Park, M. G. Kim, T.K. Ha, K.H. Chae, S. Gautam, *Phys. Chem. Chem. Phys.*, 16 (2014) 19909-19916.
20. M.A. Flores-Gonzalez, K. Lebbou, R. Bazzi, C. Louis, P. Perriat, O. Tillement, *J. Cryst. Growth*, 2005, 277, 502-508.
21. E.J. Kim, Y.C. Kang, H.D. Park, S.K. Ryu, *Mater. Res. Bull.*, 2003, 38, 515-524.
22. M. Pal, U. Pal, J. M. G. Y. Jiménez and F. P. Rodríguez, *Nanoscale Res. Lett.*, 2012, 7, 1-12.
23. S. K. Kandpal, B. Goundie, J. wright, R. A. Pollock, M. D. Mason and R. W. Meulenberg, *ACS Appl. Mater. Interfaces*, 2011, 3, 3482-3486.
24. W. C. Wang, S. Y. Chen, P. A. Glans, J. Guo, R. Chen, K. W. Fong, C. L. Chen, A. Gloter, C. Lin Chang, T.S. Chan, J. M. Chen, J. F. Leed and C. L. Dong, *Phys. Chem. Chem. Phys.*, 2013, 15, 14701-14707.
25. R. Karnatak, J. Esteva, H. Dexpert, M. Gasgnier, P. Caro and C. L. Albert, *Phys. Rev. B*, 1987, 36, 1745-1749.
26. C. L. Tracy, M. Lang, J. M. Pray, F. Zhang, D. Popov, C. Park, C. Trautmann, M. Bender, D. Severin, V. A. Skuratov and R. C. Ewing, *Nat. Commun.* 2015, 6, 6133 (1-9).
27. J. Rakovan, M. Newville and s. Sutton, *American Mineralogist*, 2001, 86, 697-700.
28. D.C. Konigsberger and R. Prince, *X-ray Absorption: Principles, Applications, Techniques of EXAFS, SEXAFS and XANES*, Wiley, New York, 1988.
29. B. Ravel and M. Newville, *J. Synchrotron Radiat.*, 2005, 12, 537-541.
30. A. L. Ankudinov and J. J. Rehr, *Phys. Rev. B*, 1997, 56, R1712-R1715.
31. J. F. Lee, M.T. Tang, W. C. Shin and R. S. Liu, *Mat. Res. Bul.*, 2002, 37, 555-562.
32. S. Tsunekawa, T. Fukuda, and A. Kasuya, *J. Appl. Phys.*, 2000, 87, 1318-1321.
33. J. Chen, J. Wang, F. Zhang, D. Yan, G. Zhang, R. Zhuo and P. Yan, *J. Phys. D: Appl. Phys.*, 2008, 41, 105306-105311.
34. C. Mao, Y. Zhao, X. Qiu, J. Zhu and C. Burda, *Phys. Chem. Chem. Phys.*, 2008, 10, 5633-5638.
35. R. Li, X. Yan, L. Yu, Z. Zhang, Q. Tang and Y. Pan, *Crys. Eng. Comm.*, 2013, 15, 10049-10058.
36. L. Pan, X. Liu, Z. Sun and C. Q. Sun, *J. Mat. Chem. A*, 2013, 1, 8299-8326.
37. S. Y. Yao, W. Q. Xu, A. C. Johnston-Peck, F. Z. Zhao, Z. Y. Liu, S. Luo, S. D. Senanayake, A. Martínez-Arias, W. J. Liu and J. A. Rodriguez, *Phys. Chem. Chem. Phys.*, 2014, 16, 17183-17195.
38. A. Hagfeldt and M. Gratzel, *Chem. Rev.*, 1995, 95, 49-68.